Utilization of Event Shape in Search of the Chiral Magnetic Effect in Heavy-ion Collisions

Ryan Milton,[1,*] Gang Wang,[1,†] Maria Sergeeva,[1] Shuzhe Shi,[2] Jinfeng Liao,[3] and Huan Zhong Huang[1,4]

[1] *Department of Physics and Astronomy, University of California, Los Angeles, California 90095, USA*
[2] *Department of Physics, McGill University, 3600 University Street, Montreal, QC, H3A 2T8, Canada*
[3] *Physics Department and Center for Exploration of Energy and Matter, Indiana University, 2401 N Milo B. Sampson Lane, Bloomington, IN 47408, USA*
[4] *Key Laboratory of Nuclear Physics and Ion-beam Application (MOE), and Institute of Modern Physics, Fudan University, Shanghai-200433, People's Republic of China*

The search for the chiral magnetic effect (CME) has been a subject of great interest in the field of high-energy heavy-ion collision physics, and various observables have been proposed to probe the CME. Experimental observables are often contaminated with background contributions arising from collective motions (specifically elliptic flow) of the collision system. We present a method study of event-shape engineering (ESE) that projects the CME-sensitive γ_{112} correlator and its variations (γ_{132} and γ_{123}) to a class of events with minimal flow. We discuss the realization of the zero-flow mode, the sensitivity on the CME signal, and the corresponding statistical significance for Au+Au, Ru+Ru, and Zr+Zr collisions at $\sqrt{s_{\rm NN}} = 200$ GeV with a multiphase transport (AMPT) model, as well as a new event generator, Event-By-Event Anomalous-Viscous Fluid Dynamics (EBE-AVFD).

I. INTRODUCTION

A major goal of the experiments on high-energy heavy-ion collisions is to produce a deconfined nuclear matter, known as the Quark-Gluon Plasma (QGP), and to study its properties. The creation of a QGP provides a test to the topological sector of quantum chromodynamics (QCD), the fundamental theory of strong interactions. According to QCD, quarks in a QGP could obtain a chirality imbalance via the chiral anomaly [1, 2], forming local domains with finite chiral chemical potentials (μ_5) [3–8]. These chiral quarks could manifest an electric current along the direction of the strong magnetic field ($\vec{B} \sim 10^{14}$ T) generated by the incident protons in the heavy-ion collisions: $\vec{J_e} \propto \mu_5 \vec{B}$, which is theorized as the chiral magnetic effect (CME) [3, 4]. Some recent reviews on the CME are available in Refs. [9–12].

On average, $\vec{B}$ is expected to be perpendicular to the reaction plane (RP), which is spanned by the impact parameter and the beam momenta of a collision. The CME will then give rise to an electric charge separation across the RP. In the study of the CME-induced charge separation as well as other collective motions in the QGP, the azimuthal distribution of produced particles is often expressed with the Fourier expansion for given transverse momentum (p_T) and pseudorapidity (η) in an event:

$$\frac{dN_\alpha}{d\phi^*} \approx \frac{N_\alpha}{2\pi}[1 + 2v_{1,\alpha}\cos(\phi^*) + 2v_{2,\alpha}\cos(2\phi^*) + 2v_{3,\alpha}\cos(3\phi^*) + ... + 2a_{1,\alpha}\sin(\phi^*) + ...\,], \quad (1)$$

where $\phi^* = \phi - \Psi_{\rm RP}$, and ϕ and $\Psi_{\rm RP}$ are the azimuthal angles of a particle and the RP, respectively. The subscript α (+ or −) denotes the particle's charge sign. Traditionally, the coefficients v_1, v_2, and v_3 are called "directed flow", "elliptic flow", and "triangular flow", respectively. In the scenario of fluid evolution, these v_n coefficients reflect the hydrodynamic response of the QGP to the initial collision geometry and to its fluctuations [13]. Figure 1 sketches the transverse plane, perpendicular to the beam direction (the $z_{\rm lab}$ axis), in an off-center heavy-ion collision. In practice, an event plane obtained from the collective motion of detected particles is used instead of the true RP. For simplicity, we still use the RP notation in the following discussions, and RP could represent a specific event plane.

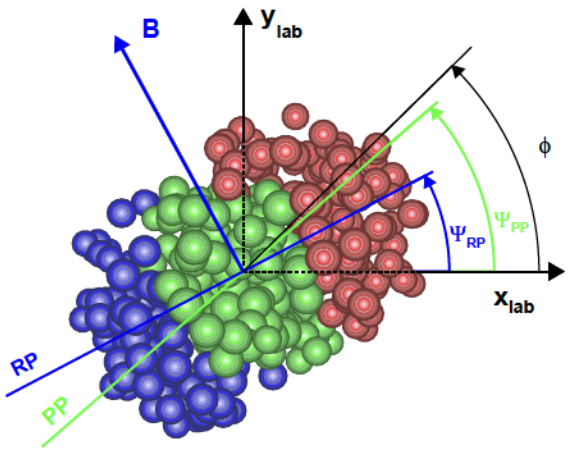

Fig. 1: Schematic diagram of the transverse plane for a two-nucleus collision, with the left one emerging from and the right one going into the page. Particles are produced in the overlap region (green-colored participating nucleons). The azimuthal angles of the reaction plane ($\Psi_{\rm RP}$), the participant plane ($\Psi_{\rm PP}$), and a produced particle (ϕ) are depicted here.

The a_1 coefficient (with $a_{1,+} \approx -a_{1,-}$ in a charge-symmetric system) quantifies the CME-induced charge

* rmilton@ucla.edu
† gwang@physics.ucla.edu

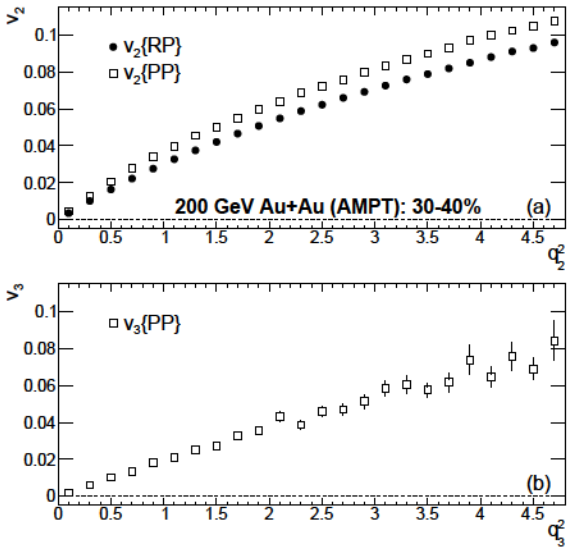

Fig. 2: AMPT simulations of v_2 vs q_2^2 (a) and v_3 vs q_3^2 (b) for 30–40% Au+Au collisions at $\sqrt{s_{\rm NN}} = 200$ GeV.

partonic evolution, the spatial quark coalescence is implemented to attain the quark-hadron phase transition in the string melting (SM) version of AMPT. Finally, the hadronic interactions are modelled by A Relativistic Transport calculations (ART) [38].

The SM version of AMPT reasonably well reproduces particle spectra and elliptic flow in Au+Au collisions at 200 GeV and Pb+Pb collisions at 2.76 TeV [39]. In this study, the SM v2.25t4cu of AMPT has been used to simulate 2.4×10^7 events of 0–80% Au+Au collisions at $\sqrt{s_{\rm NN}} = 200$ GeV. This version conserves electric charge, which is particularly important for the CME-related analyses. The model parameters are set in the same way as in Ref. [27]. Only $\pi^{\pm}$, $K^{\pm}$, p and $\bar{p}$ are included in the following simulations.

Figure 2 demonstrates the effectiveness of q_2^2 and q_3^2 in characterizing the event shape with AMPT calculations of $v_2(q_2^2)$ (a) and $v_3(q_3^2)$ (b), respectively, for the 30–40% centrality interval in Au+Au collisions at $\sqrt{s_{\rm NN}} = 200$ GeV. Although the v_2 values with respect to the RP and the PP are different because of the fluctuation of the initial nucleons, they both approach zero at $q_2^2 = 0$. In a similar way, the zero-v_3 mode is also realized at vanishing q_3^2. The q_2^2 and q_3^2 ranges under study have covered 86.2% and 98.5% of the whole event sample, respectively.

Figures 3 and 4 illustrate how the zero-flow mode is accomplished for $\Delta\gamma_{112}$ and $\Delta\gamma_{132}$, respectively, via q_2^2 (a), v_2 (b), and $v_2\Delta\delta$ (c) with AMPT events of 30–40% Au+Au collisions at $\sqrt{s_{\rm NN}} = 200$ GeV. Each panel contains results with respect to both the RP and the PP, which are fit with second-order polynomial functions in panel (a), and with linear functions in panels (b) and (c). The solid (dashed) lines represent the fit functions to the results with respect to the RP (PP). In panel (a), the solid and dashed lines are significantly different, since the flow-related background is proportional to v_2, and

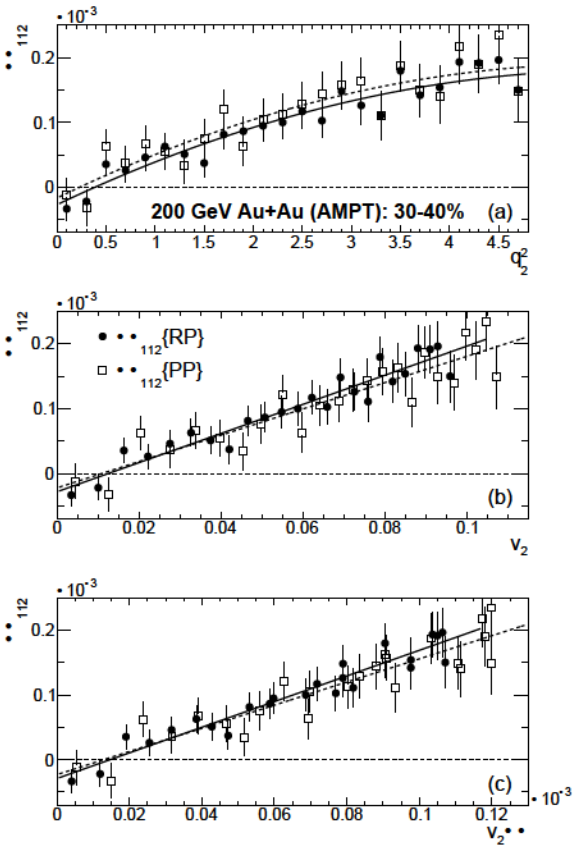

Fig. 3: AMPT calculations of $\Delta\gamma_{112}$ as a function of q_2^2 (a), v_2 (b), and $v_2\Delta\delta$ (c) for 30–40% Au+Au collisions at $\sqrt{s_{\rm NN}} = 200$ GeV. The results are fit with second-order polynomial functions in panel (a), and with linear functions in panels (b) and (c).

$v_2\{\mathrm{RP}\}$ is different from $v_2\{\mathrm{PP}\}$, as shown in Fig. 2(a). In panels (b) and (c), where v_2 explicitly appears on the horizontal axis, the difference between the solid and dashed lines is suppressed. The vertical intercepts of all the fit functions are close to zero, but slightly negative, indicating a potential over-correction of the flow-related background. The centrality dependence of these intercepts will be discussed later in Figure 6.

Figure 5 exhibits $\Delta\gamma_{123}$ with respect to the PP vs q_3^2 (a), v_3 (b), and $v_3\Delta\delta$ (c), calculated with AMPT events of 30–40% Au+Au collisions at $\sqrt{s_{\rm NN}} = 200$ GeV. The results are fit with a second-order polynomial function in panel (a), and with linear functions in panels (b) and (c). Unlike the cases of $\Delta\gamma_{112}$ and $\Delta\gamma_{112}$, $\Delta\gamma_{123}$ does not diminish at the zero-flow mode, but stays rather constant as a function of either q_3^2, v_3, or $v_3\Delta\delta$. This implies that the formation of the finite $\Delta\gamma_{123}$ arises from a different mechanism than either $\Delta\gamma_{132}$ or the flow-induced background in $\Delta\gamma_{112}$.

We have applied the same analysis procedure as in Figs. 3, 4, and 5 to different centrality classes. Figure 6 shows the centrality dependence of $\Delta\gamma_{112}$ (a) and $\Delta\gamma_{132}$ (b) with respect to the RP at the zero-flow mode for AMPT events of Au+Au collisions at $\sqrt{s_{\rm NN}} = 200$ GeV.

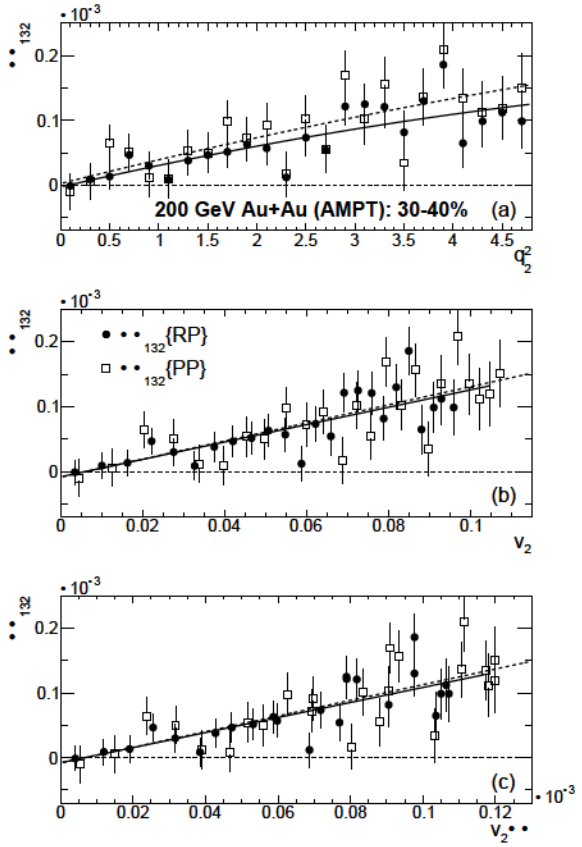

Fig. 4: AMPT simulations of $\Delta\gamma_{132}$ as a function of q_2^2 (a), v_2 (b), and $v_2\Delta\delta$ (c) for 30–40% Au+Au collisions at $\sqrt{s_{\rm NN}} = 200$ GeV. The results are fit with second-order polynomial functions in panel (a), and with linear functions in panels (b) and (c).

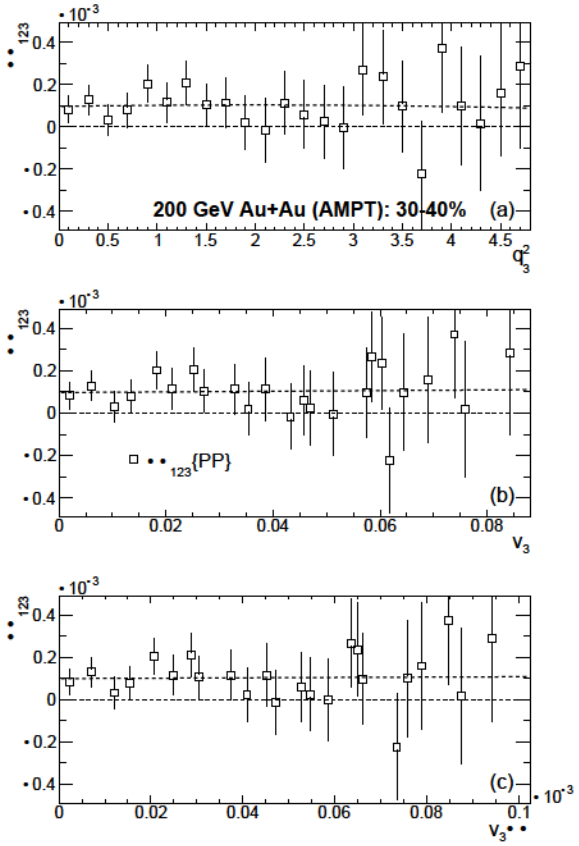

Fig. 5: AMPT calculations of $\Delta\gamma_{123}$ as a function of q_3^2 (a), v_3 (b), and $v_3\Delta\delta$ (c) for 30–40% Au+Au collisions at $\sqrt{s_{\rm NN}} = 200$ GeV. The results are fit with a second-order polynomial function in panel (a), and with linear functions in panels (b) and (c).

The open markers represent the fit intercepts via different variables: q_2^2, v_2, and $v_2\Delta\delta$. At each centrality interval, the three intercepts are consistent with each other, and are consistent with or lower than zero. Therefore, the zero-flow projection in AMPT events demonstrates similar efficacy in removing the flow-related background in $\Delta\gamma_{112}$ and $\Delta\gamma_{132}$. In comparison, the ensemble averages are also drawn with the solid markers. Using the ensemble averages as a reference baseline, we illustrate how much background contributions have been suppressed with the ESE technique, and also visualize the potential over-subtraction of background in some centrality ranges.

Figure 7 displays the centrality dependence of $\Delta\gamma_{112}$ (a), $\Delta\gamma_{132}$ (b), and $\Delta\gamma_{123}$ (c) with respect to the PP at the zero-flow mode for AMPT events of Au+Au collisions at $\sqrt{s_{\rm NN}} = 200$ GeV. The open markers represent the fit intercepts via different variables: q_n^2, v_n, and $v_n\Delta\delta$. The ensemble averages are also added with the solid markers in comparison. In general, the results for $\Delta\gamma_{112}\{\rm PP\}$ and $\Delta\gamma_{132}\{\rm PP\}$ qualitatively resemble those for $\Delta\gamma_{112}\{\rm RP\}$ and $\Delta\gamma_{132}\{\rm RP\}$, respectively. Therefore, the ESE method seems to work regardless of the event-plane type. We will further perform these analyses to the EBE-AVFD events in the following subsection to investigate whether the over-subtraction of background is model-dependent or a universal feature of this ESE approach. The intercepts for $\Delta\gamma_{123}\{\rm PP\}$ are consistent with the ensemble average for the centrality range under study, indicating the failure of this ESE recipe for this observable. This observation seems to echo the conclusion in Ref. [27] that the underlying mechanism for $\Delta\gamma_{123}$ is different from that for the flow-related background in $\Delta\gamma_{112}$, and thus $\Delta\gamma_{123}$ is not a good background estimate for $\Delta\gamma_{112}$.

It is remarkable that for all the aforementioned results, the intercepts via q_n^2 as the variable bear larger statistical uncertainties than those via the other two (v_n and $v_n\Delta\delta$), though they are all consistent with each other. This mostly results from the different fit functions to extract the intercepts. Therefore, v_n and $v_n\Delta\delta$ are technically preferred over q_n^2 in projection of these $\Delta\gamma$ correlators to the zero-flow mode.

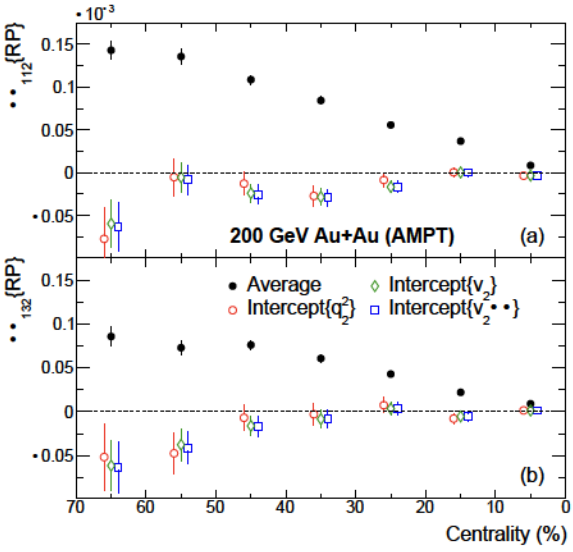

Fig. 6: Centrality dependence of $\Delta\gamma_{112}\{\mathrm{RP}\}$ (a) and $\Delta\gamma_{132}\{\mathrm{RP}\}$ (b) at the zero-flow mode for AMPT events of Au+Au collisions at $\sqrt{s_{\mathrm{NN}}} = 200$ GeV. The open markers represent the fit intercepts via different variables: q_2^2, v_2, and $v_2\Delta\delta$. In comparison, the ensemble averages are also drawn with the solid markers.

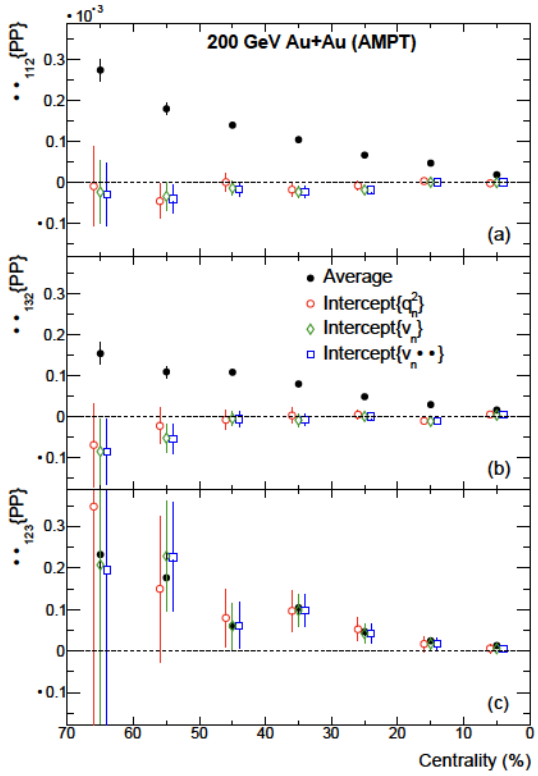

Fig. 7: Centrality dependence of $\Delta\gamma_{112}\{\mathrm{PP}\}$ (a), $\Delta\gamma_{132}\{\mathrm{PP}\}$ (b), and $\Delta\gamma_{123}\{\mathrm{PP}\}$ (c) at the zero-flow mode for AMPT events of Au+Au collisions at $\sqrt{s_{\mathrm{NN}}} = 200$ GeV. The open markers represent the fit intercepts via different variables: q_n^2, v_n, and $v_n\Delta\delta$. In comparison, the ensemble averages are also drawn with the solid markers.

B. EBE-AVFD

The EBE-AVFD model [29–31] is a comprehensive simulation framework that describes the dynamical CME transport for quark currents in addition to the relativistically expanding viscous QGP fluid, and properly models major sources of background correlations, such as LCC and resonance decays.

The initial conditions for entropy density (s) profiles and the initial electromagnetic field are fluctuated according to the event-by-event nucleon configuration in the Monte Carlo Glauber simulations [40]. The initial axial charge density (n_5) is introduced as being proportional to the corresponding local entropy density with a constant ratio. This ratio parameter can be varied to control the strength of the CME transport. For example, one can set n_5/s to 0, 0.1, and 0.2, to simulate scenarios of zero, modest, and strong CME signals, respectively.

The hydrodynamic evolution is solved through two components: the bulk-matter collective flow and the dynamical CME transport. The former is managed by the VISH2+1 simulation package [41], which has been extensively tested and validated with relevant experimental data. The latter is described by anomalous hydrodynamic equations for the quark chiral currents on top of the bulk flow background. The magnetic-field-induced CME currents lead to a charge separation in the fireball. Additionally, the conventional transport processes like diffusion and relaxation for the quark currents are coherently included, and relevant details can be found in Refs. [29–31].

In the freeze-out process, the LCC effect is implemented by producing some charged hadron-antihadron pairs from the same fluid cell, with their momenta sampled independently in the local rest frame of the cell. In this study, a parameter of $P_{\mathrm{LCC}} = 1/3$ is set to characterize the fraction of charged hadrons that are sampled in oppositely-charged pairs, while the rest of the hadrons are sampled independently. Finally, all the hadrons produced from the freeze-out hypersurface are further subject to hadron cascades through the UrQMD simulations [42], which account for various hadron resonance decay processes and automatically carry their contributions to the charge-dependent correlations.

1. *Au+Au collisions at* $\sqrt{s_{\mathrm{NN}}} = 200$ *GeV*

Figure 8 depicts the EBE-AVFD calculations of $\Delta\gamma_{112}\{\mathrm{RP}\}$ and $\Delta\gamma_{112}\{\mathrm{PP}\}$ as a function of v_2 for n_5/s of 0 (a), 0.1 (b), and 0.2 (c) in 30–40% Au+Au collisions at $\sqrt{s_{\mathrm{NN}}} = 200$ GeV. The numbers of events are 9.6×10^7, 5.9×10^7, and 7.7×10^7 for the cases of $n_5/s = 0$, 0.1, and 0.2, respectively. Note that the events are still binned with q_2^2 as done in the previous subsection. The solid (dashed) lines represent the linear fit functions to the results with respect to the RP (PP). In the pure-background case ($n_5/s = 0$), the intercepts are positively

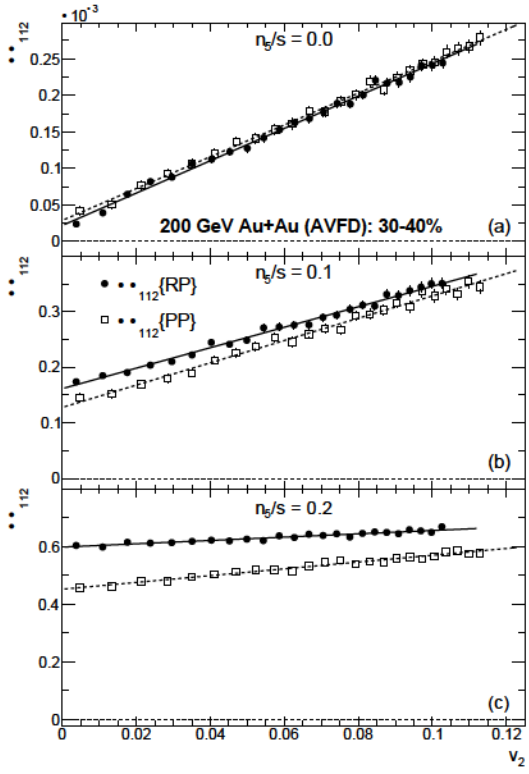

Fig. 8: EBE-AVFD calculations of $\Delta\gamma_{112}$ as a function of v_2 for n_5/s of 0 (a), 0.1 (b), and 0.2 (c) in 30–40% Au+Au collisions at $\sqrt{s_{\rm NN}} = 200$ GeV. The results are fit with linear functions.

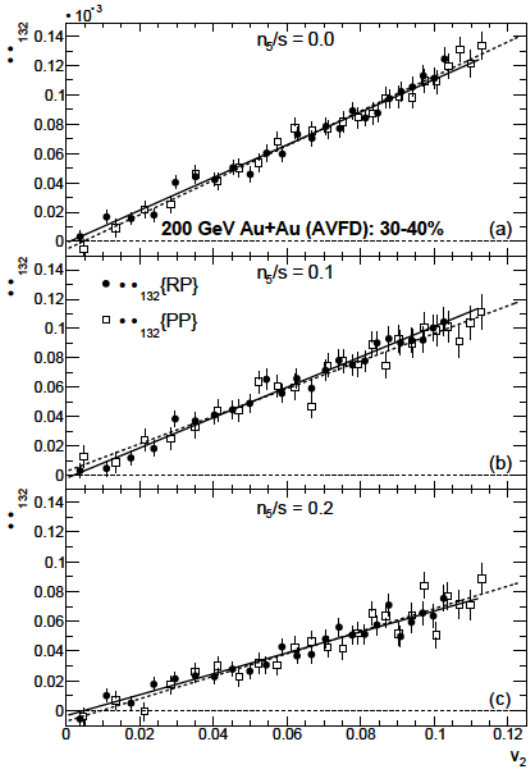

Fig. 9: EBE-AVFD simulations of $\Delta\gamma_{132}$ as a function of v_2 for n_5/s of 0 (a), 0.1 (b), and 0.2 (c) in 30–40% Au+Au collisions at $\sqrt{s_{\rm NN}} = 200$ GeV. The results are fit with linear functions.

finite, indicating that the flow-related background in the EBE-AVFD model cannot be completely removed by this ESE approach. The magnitude of the intercept increases with increasing n_5/s, meeting the CME expectation. At finite n_5/s values, $\Delta\gamma_{112}\{\rm RP\}$ is above $\Delta\gamma_{112}\{\rm PP\}$, as the RP is more closely correlated with the magnetic-field direction, and hence $\Delta\gamma_{112}\{\rm RP\}$ contains a larger CME signal than $\Delta\gamma_{112}\{\rm PP\}$. For simplicity, we do not show the similar results as a function of q_2^2 or $v_2\Delta\delta$, but the corresponding intercepts will be presented in Fig. 11.

Figure 9 delineates the EBE-AVFD simulations of $\Delta\gamma_{132}\{\rm RP\}$ and $\Delta\gamma_{132}\{\rm PP\}$ as a function of v_2 for n_5/s of 0 (a), 0.1 (b), and 0.2 (c) in 30–40% Au+Au collisions at $\sqrt{s_{\rm NN}} = 200$ GeV. For all the n_5/s values under study, the intercept of the linear fit is always consistent with zero. Similar intercept results extracted via q_2^2 or $v_2\Delta\delta$ will be summarized in Fig. 12.

Figure 10 presents the EBE-AVFD calculations of $\Delta\gamma_{123}\{\rm PP\}$ as a function of v_3 for n_5/s of 0 (a), 0.1 (b), and 0.2 (c) in 30–40% Au+Au collisions at $\sqrt{s_{\rm NN}} = 200$ GeV. Note that the events are still binned with q_3^2 as done in the previous subsection. The intercept of the linear fit seems to decrease with increasing n_5/s, which will be further discussed in Fig. 13, together with similar intercept results extracted via q_3^2 and $v_3\Delta\delta$.

We extract the ESE intercepts of $\Delta\gamma_{112}\{\rm RP\}$ and $\Delta\gamma_{112}\{\rm PP\}$ via q_2^2, v_2, and $v_2\Delta\delta$, for EBE-AVFD events of 30–40% Au+Au collisions at $\sqrt{s_{\rm NN}} = 200$ GeV, and present the results corrected with $(1-2v_2)$ as a function of n_5/s in Fig. 11. The conventional ensemble average values are also shown in comparison. In the pure-background scenario ($n_5/s = 0$), although the ESE intercepts do not completely remove the residue background, they do suppress the background contribution roughly by a factor of 6 relative to the ensemble average for both $\Delta\gamma_{112}\{\rm RP\}$ and $\Delta\gamma_{112}\{\rm PP\}$. In the cases of finite n_5/s values, we estimate the CME contribution in two ways. As pointed out in Ref. [19], with $\Psi_{\rm RP}$ known in the model, we can directly calculate $a_{1,\pm}$, and utilize the following relation to estimate the CME contribution in $\Delta\gamma_{112}\{\rm RP\}$:

$$\begin{aligned}&\Delta\gamma_{112}^{\rm CME}\{\rm RP\}\\ &= \Delta\gamma_{112}\{\rm RP\} - \Delta\gamma_{112}\{\rm RP\}|_{n_5/s=0} \qquad (9)\\ &= (a_{1,+}^2 + a_{1,-}^2)/2 - a_{1,+}a_{1,-}. \qquad (10)\end{aligned}$$

In Fig. 11(a), the solid line stands for a second-order polynomial fit to the quantity in Eq. (9), whereas the dashed line denotes that to the quantity in Eq. (10). The good consistency between the two estimates corroborates the relation in Eqs. (9) and (10). In Fig. 11(b), where the PP is used in the analysis, only the solid line is drawn to represent $(\Delta\gamma_{112}\{\rm PP\} - \Delta\gamma_{112}\{\rm PP\}|_{n_5/s=0})$. In all the cases, the ESE results are much closer to the true CME signal than the ensemble average.

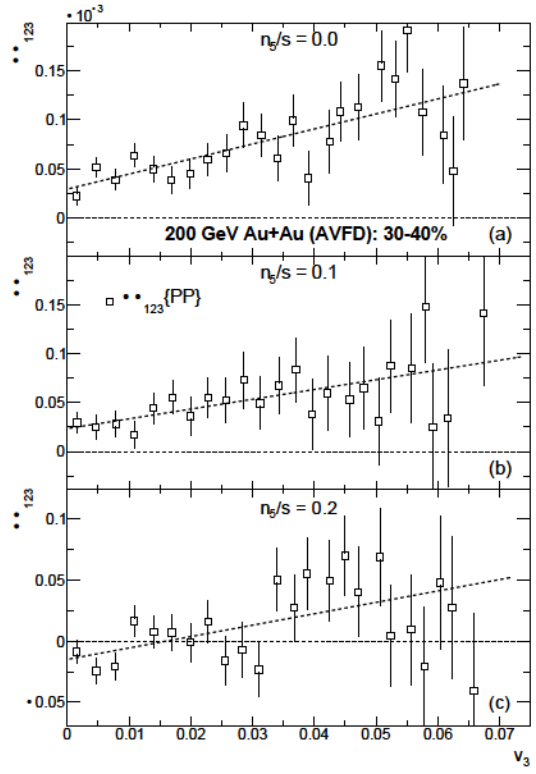

Fig. 10: EBE-AVFD calculations of $\Delta\gamma_{123}$ as a function of v_3 for n_5/s of 0 (a), 0.1 (b), and 0.2 (c) in 30–40% Au+Au collisions at $\sqrt{s_{\rm NN}} = 200$ GeV. The results are fit with linear functions.

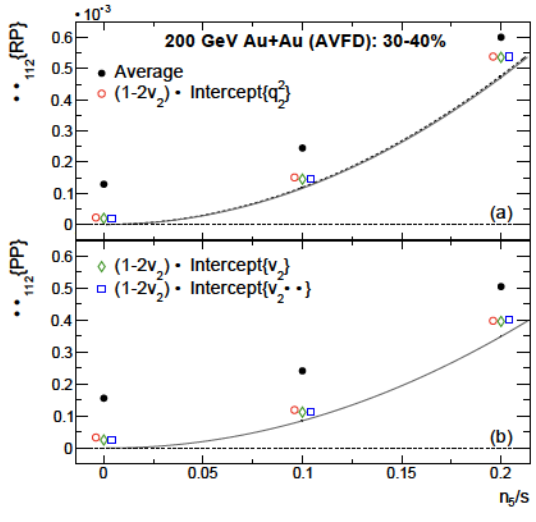

Fig. 11: n_5/s dependence of $\Delta\gamma_{112}\{\rm RP\}$ (a) and $\Delta\gamma_{112}\{\rm PP\}$ (b) at the zero-flow mode for EBE-AVFD events of 30–40% Au+Au collisions at $\sqrt{s_{\rm NN}} = 200$ GeV. The open markers represent the fit intercepts via different variables: q_2^2, v_2, and $v_2\Delta\delta$. In comparison, the ensemble averages are also drawn with the solid markers. The solid and dashed lines are estimates for the CME signal, and are explained in the text.

With the estimated $\Delta\gamma_{112}^{\rm CME}$ values, we can easily calculate the fraction of the CME signal, $f_{\rm CME}$, in the ensemble average of $\Delta\gamma_{112}$ as well as in the corrected ESE intercepts. Table I lists the EBE-AVFD calculations of $f_{\rm CME}$ for different observables in 30–40% Au+Au collisions at $\sqrt{s_{\rm NN}} = 200$ GeV, for $n_5/s = 0.1$ and 0.2. In general, $f_{\rm CME}$ increases with increasing n_5/s, as expected. The values of $f_{\rm CME}\{\rm RP\}$ for the ensemble averages are significantly larger than those of $f_{\rm CME}\{\rm PP\}$ as explained before: the smaller $v_2\{\rm RP\}$ values cause smaller flow-induced backgrounds, whereas the RP is more closely correlated with the magnetic-field direction, leading to larger CME signals. The difference between $f_{\rm CME}\{\rm RP\}$ and $f_{\rm CME}\{\rm PP\}$ is reduced for the ESE intercepts, since the background is largely suppressed. At $n_5/s = 0.2$ where the CME signal is very strong, $f_{\rm CME}$ could reach around 88% for the ESE intercepts, and drop by 10–20% for the ensemble average depending on whether the RP or the PP is used. With weaker CME signals at $n_5/s = 0.1$, the advantage of the ESE intercepts over the ensemble average becomes more prominent in $f_{\rm CME}$. On the other hand, the disadvantage of the ESE approach is also clear: the statistical uncertainty is about 2–4 times larger than that of the ensemble average.

Table I: The fraction of the CME signal, $f_{\rm CME}$, for the ensemble average of $\Delta\gamma_{112}$ and the corrected ESE intercepts in EBE-AVFD events of 30–40% Au+Au collisions at $\sqrt{s_{\rm NN}} = 200$ GeV, for $n_5/s = 0.1$ and 0.2.

$n_5/s = 0.1$	Average	ESE$\{q_2^2\}$	ESE$\{v_2\}$	ESE$\{v_2\Delta\delta\}$
$f_{\rm CME}\{\rm RP\}$ (%)	47.4±0.5	76.9±1.7	80.0±1.6	79.3±1.5
$f_{\rm CME}\{\rm PP\}$ (%)	35.4±0.6	71.7±2.7	76.2±2.6	75.1±2.5
$n_5/s = 0.2$	Average	ESE$\{q_2^2\}$	ESE$\{v_2\}$	ESE$\{v_2\Delta\delta\}$
$f_{\rm CME}\{\rm RP\}$ (%)	78.5±0.2	87.5±0.5	87.9±0.4	87.6±0.4
$f_{\rm CME}\{\rm PP\}$ (%)	69.1±0.3	87.7±0.8	88.1±0.7	86.9±0.7

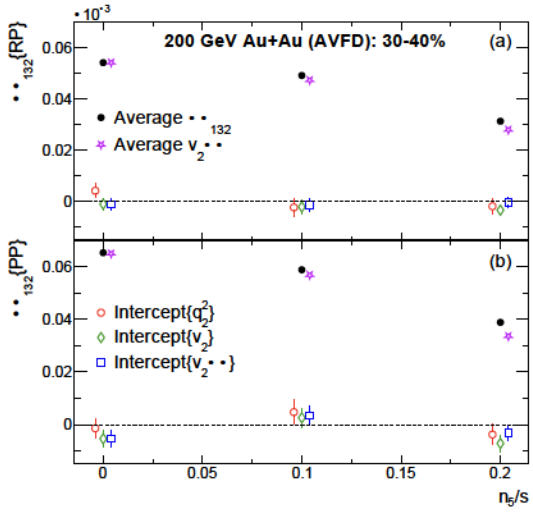

Fig. 12: n_5/s dependence of $\Delta\gamma_{132}\{\rm PP\}$ (a) and $\Delta\gamma_{132}\{\rm PP\}$ (b) at the zero-flow mode for EBE-AVFD events of 30–40% Au+Au collisions at $\sqrt{s_{\rm NN}} = 200$ GeV. The open markers represent the fit intercepts via different variables: q_2^2, v_2, and $v_2\Delta\delta$. In comparison, the ensemble averages for $\Delta\gamma_{132}$ and $v_2\Delta\delta$ are also drawn.

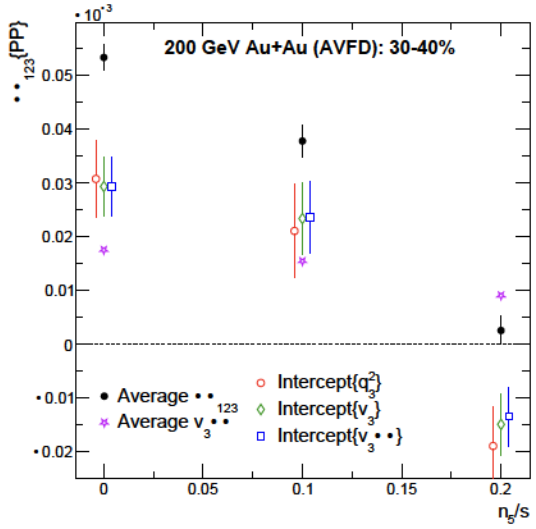

Fig. 13: n_5/s dependence of $\Delta\gamma_{123}\{\mathrm{PP}\}$ at the zero-flow mode for EBE-AVFD events of 30–40% Au+Au collisions at $\sqrt{s_{\mathrm{NN}}} = 200$ GeV. The open markers represent the fit intercepts via different variables: q_3^2, v_3, and $v_3\Delta\delta$. In comparison, the ensemble averages for $\Delta\gamma_{123}$ and $v_3\Delta\delta$ are also drawn.

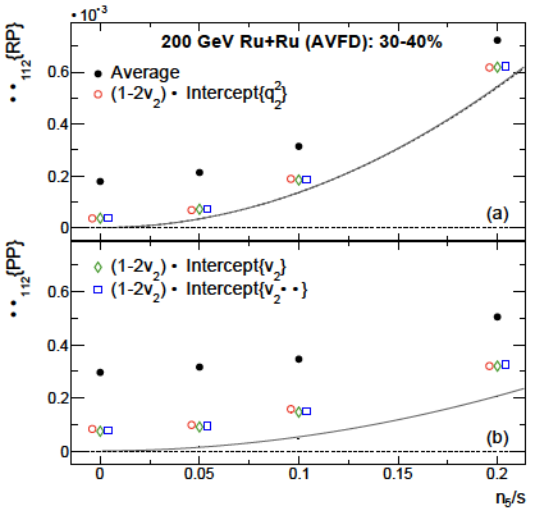

Fig. 14: n_5/s dependence of $\Delta\gamma_{112}\{\mathrm{RP}\}$ (a) and $\Delta\gamma_{112}\{\mathrm{PP}\}$ (b) at the zero-flow mode for EBE-AVFD events of 30–40% Ru+Ru collisions at $\sqrt{s_{\mathrm{NN}}} = 200$ GeV. The open markers represent the fit intercepts via different variables: q_2^2, v_2, and $v_2\Delta\delta$. In comparison, the ensemble averages are also drawn with the solid markers. The solid and dashed lines are estimates for the CME signal, as explained in the text.

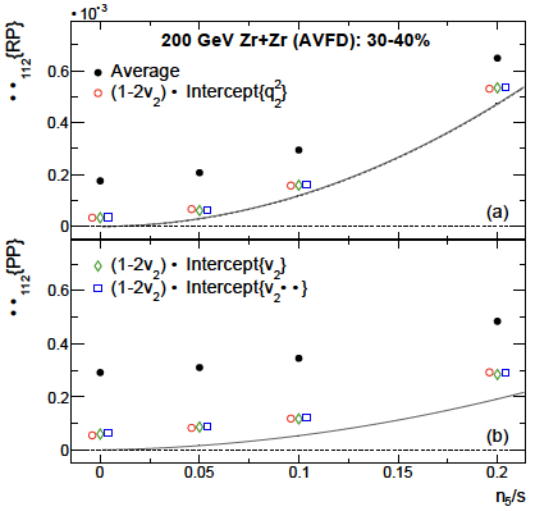

Fig. 15: n_5/s dependence of $\Delta\gamma_{112}\{\mathrm{RP}\}$ (a) and $\Delta\gamma_{112}\{\mathrm{PP}\}$ (b) at the zero-flow mode for EBE-AVFD events of 30–40% Zr+Zr collisions at $\sqrt{s_{\mathrm{NN}}} = 200$ GeV. The open markers represent the fit intercepts via different variables: q_2^2, v_2, and $v_2\Delta\delta$. In comparison, the ensemble averages are also drawn with the solid markers. The solid and dashed lines are estimates for the CME signal, as explained in the text.

Figure 12 shows the n_5/s dependence of $\Delta\gamma_{132}\{\mathrm{PP}\}$ (a) and $\Delta\gamma_{132}\{\mathrm{PP}\}$ (b) at the zero-flow mode for EBE-AVFD events of 30–40% Au+Au collisions at $\sqrt{s_{\mathrm{NN}}} = 200$ GeV. The ensemble average values for $\Delta\gamma_{132}$ and $v_2\Delta\delta$ are also drawn in comparison. Unlike the case of $\Delta\gamma_{112}$, $\Delta\gamma_{132}$ seems to vanish with the ESE technique in most cases, supporting the idea that $\Delta\gamma_{132}$ is approximately equal to $v_2\Delta\delta$ [27], and hence should disappear at the zero-flow mode. The equivalence relation between $\Delta\gamma_{132}$ and $v_2\Delta\delta$ also explains why the ensemble average of $\Delta\gamma_{132}$ decreases with increasing n_5/s: v_2 is basically constant over n_5/s, and $\Delta\delta$ is expected to decrease with increasing n_5/s [31]. Therefore, in the real-data analyses, $\Delta\gamma_{132}$ can be used as a systematic check on how well the ESE approach works in terms of the background removal.

Figure 13 shows the n_5/s dependence of $\Delta\gamma_{123}\{\mathrm{PP}\}$ at the zero-flow mode for EBE-AVFD events of 30–40% Au+Au collisions at $\sqrt{s_{\mathrm{NN}}} = 200$ GeV, with the ensemble averages for $\Delta\gamma_{123}$ and $v_3\Delta\delta$ drawn in comparison. Both the ESE intercepts and the ensemble average for $\Delta\gamma_{123}$ have a stronger dependence on n_5/s than $v_3\Delta\delta$. The flow-related contributions in $\Delta\gamma_{123}$ seem to be reduced by the ESE technique, but they do not disappear as in the case of $\Delta\gamma_{132}$. Although a further investigation is needed to better understand the mechanism behind $\Delta\gamma_{123}$, we can draw a similar conclusion as in Ref. [27] that $\Delta\gamma_{123}$ is not a proper background estimate for $\Delta\gamma_{112}$.

2. *Ru+Ru and Zr+Zr collisions at* $\sqrt{s_{\mathrm{NN}}} = 200$ *GeV*

Recently the STAR Collaboration has completed the blind analysis of the isobar-collision data, without observing any predefined CME signature [43]. One possibility is that f_{CME} is much smaller in Ru+Ru and Zr+Zr than in Au+Au at the same n_5/s [45]. We shall explore both the conventional ensemble average and the ESE intercepts for $\Delta\gamma_{112}$ along this direction with EBE-AVFD simulations. With our current precision, the results for Ru+Ru and Zr+Zr are consistent with each other for all the cases. The differentiation of the two isobaric systems

Table II: $f_{\rm CME}$ for the ensemble average of $\Delta\gamma_{112}$ and the corrected ESE intercepts in EBE-AVFD events of 30–40% Ru+Ru collisions at $\sqrt{s_{\rm NN}} = 200$ GeV, for $n_5/s = 0.05$, 0.1, and 0.2.

$n_5/s = 0.05$	Average	ESE$\{q_2^2\}$	ESE$\{v_2\}$	ESE$\{v_2\Delta\delta\}$
$f_{\rm CME}\{\rm RP\}$ (%)	16.3±1.7	51.0±6.7	48.5±5.8	47.2±5.5
$f_{\rm CME}\{\rm PP\}$ (%)	6.3±2.1	20.2±7.1	21.8±7.5	21.1±7.3
$n_5/s = 0.1$	Average	ESE$\{q_2^2\}$	ESE$\{v_2\}$	ESE$\{v_2\Delta\delta\}$
$f_{\rm CME}\{\rm RP\}$ (%)	43.2±1.4	71.9±3.5	73.6±3.1	72.7±3.1
$f_{\rm CME}\{\rm PP\}$ (%)	14.4±2.2	31.3±5.7	33.7±5.9	33.0±5.7
$n_5/s = 0.2$	Average	ESE$\{q_2^2\}$	ESE$\{v_2\}$	ESE$\{v_2\Delta\delta\}$
$f_{\rm CME}\{\rm RP\}$ (%)	75.3±0.5	88.2±0.9	88.0±0.8	87.6±0.7
$f_{\rm CME}\{\rm PP\}$ (%)	41.3±1.3	65.0±2.8	65.1±2.5	63.9±2.4

Table III: $f_{\rm CME}$ for the ensemble average of $\Delta\gamma_{112}$ and the corrected ESE intercepts in EBE-AVFD events of 30–40% Zr+Zr collisions at $\sqrt{s_{\rm NN}} = 200$ GeV, for $n_5/s = 0.05$, 0.1, and 0.2.

$n_5/s = 0.05$	Average	ESE$\{q_2^2\}$	ESE$\{v_2\}$	ESE$\{v_2\Delta\delta\}$
$f_{\rm CME}\{\rm RP\}$ (%)	15.2±1.7	46.9±6.7	51.3±7.0	49.8±6.7
$f_{\rm CME}\{\rm PP\}$ (%)	6.1±2.2	22.5±8.7	21.7±8.2	21.0±7.9
$n_5/s = 0.1$	Average	ESE$\{q_2^2\}$	ESE$\{v_2\}$	ESE$\{v_2\Delta\delta\}$
$f_{\rm CME}\{\rm RP\}$ (%)	40.3±1.1	75.4±2.8	74.7±2.5	73.3±2.4
$f_{\rm CME}\{\rm PP\}$ (%)	15.5±1.7	45.1±5.9	45.6±5.7	43.7±5.4
$n_5/s = 0.2$	Average	ESE$\{q_2^2\}$	ESE$\{v_2\}$	ESE$\{v_2\Delta\delta\}$
$f_{\rm CME}\{\rm RP\}$ (%)	72.9±0.6	89.1±1.0	88.5±0.9	88.0±0.9
$f_{\rm CME}\{\rm PP\}$ (%)	39.8±1.3	65.8±3.1	67.7±2.9	66.4±2.8

[1] S. L. Adler, Phys. Rev. , 2426 (1969).
[2] J. S. Bell and R. Jackiw, Nuovo Cim. A , 47 (1969).
[3] D. Kharzeev, Phys. Lett. B , 260 (2006).
[4] D. E. Kharzeev, L. D. McLerran and H. J. Warringa, Nucl. Phys. A , 227 (2008).
[5] D. Kharzeev and A. Zhitnitsky, Nucl. Phys. A , 67 (2007).
[6] D. Kharzeev, A. Krasnitz and R. Venugopalan, Phys. Lett. B , 298 (2002).
[7] I. Iatrakis, S. Lin and Y. Yin, Phys. Rev. Lett. , 252301 (2015).
[8] K. Fukushima, D. E. Kharzeev and H. J. Warringa, Phys. Rev. Lett. , 212001 (2010).
[9] D.E. Kharzeev, J. Liao, S.A. Voloshin and G. Wang, Prog. Part. Nucl. Phys. , 1 (2016).
[10] Jie Zhao and Fuqiang Wang, Prog. Part. Nucl. Phys. , 200 (2019).
[11] Wei Li and Gang Wang, Annual Review of Nuclear and Particle Science , no.1, 293 (2020).
[12] D. E. Kharzeev and J. Liao, Nature Rev. Phys. , no.1, 55-63 (2021).
[13] U. Heinz and R. Snellings, Ann. Rev. Nucl. Part. Sci. , 123 (2013).
[14] S.A. Voloshin, Phys. Rev. C, , 057901 (2004).
[15] N. N. Ajitanand, R. A. Lacey, A. Taranenko and J. M. Alexander, Phys. Rev. C , 011901(R) (2011).
[16] N. Magdy, S.Z. Shi, J.F Liao, N.N Ajitanand and R.A. Lacey, Phys. Rev. C, , 061901 (2018).
[17] A.H. Tang, Chin. Phys. C, , No.5 054101 (2020).
[18] Y.F. Lin [STAR Collaboration], Nucl. Phys. A , 121828 (2021).
[19] S. Choudhury *et al.*, arXiv:2105.06044.
[20] S. Schlichting and S. Pratt, Phys. Rev. C , 014913 (2011).
[21] F. Wang, Phys. Rev. C , 064902 (2010).
[22] A. Bzdak, V. Koch and J. Liao, Lect. Notes Phys. , 503 (2013).
[23] S. Pratt, S. Schlichting and S. Gavin, Phys. Rev. C , 024909 (2011).
[24] F. Wen, J. Bryon, L. Wen and G. Wang, Chin. Phys. C , 014001 (2018).
[25] J. Bloczynski, X. G. Huang, X. Zhang and J. Liao, Phys. Lett. B , 1529(2013).
[26] A. M. Sirunyan *et al.* [CMS Collaboration], Phys. Rev.

C , 044912 (2018).
[27] S. Choudhury, G. Wang, W. B. He, Y. Hu and H. Z. Huang, Eur. Phys. J. C , 383 (2020).
[28] Z.-W. Lin, C.M. Ko, B.-A. Li, B. Zhang, S. Pal, Phys. Rev. C , 064901 (2005).
[29] S. Shi, Y. Jiang, E. Lilleskov and J. Liao, Annals Phys. , 50 (2018).
[30] Y. Jiang, S. Shi, Y. Yin and J. Liao, Chin. Phys. C , no. 1, 011001 (2018).
[31] S. Shi, H. Zhang, D. Hou and J. Liao, Phys. Rev. Lett. , 242301 (2020).
[32] S. A. Voloshin, Phys. Rev. Lett. , 172301 (2010).
[33] W.-T. Deng, X.-G. Huang, G.-L. Ma, G. Wang, Phys. Rev. C , 041901 (2016).
[34] W.-T. Deng, X.-G. Huang, G.-L. Ma, G. Wang, Phys. Rev. C , 044901 (2018).
[35] F. Wang and J. Zhao, Phys. Rev. C , 051901 (2017).
[36] X.-N. Wang, M. Gyulassy, Phys. Rev. D , 3501 (1991).
[37] B. Zhang, Comput. Phys. Commun. , 193 (1998).
[38] B. A. Li and C. M. Ko, Phys. Rev. C , 2037 (1995).
[39] Zi-Wei Lin, Phys. Rev. C , 014904 (2014).
[40] B.B. Back *et al.*, Phys. Rev. C , 031901(R) (2002); K. Adcox *et al.*, Phys. Rev. Lett. , 3500 (2001); I.G. Bearden *et al.*, Phys. Lett. B , 227 (2001); J. Adams *et al.*, arXiv:nucl-ex/0311017.
[41] C. Shen, Z. Qiu, H. Song, J. Bernhard, S. Bass and U. Heinz, Comput. Phys. Commun. , 61 (2016).
[42] M. Bleicher, E. Zabrodin, C. Spieles, S. A. Bass, C. Ernst, S. Soff, L. Bravina, M. Belkacem, H. Weber and H. Stöcker, J. Phys. G , 1859 (1999).
[43] M. S. Abdallah *et al.* [STAR Collaboration], arXiv:2109.00131.
[44] G. L. Ma and B. Zhang, Phys. Lett. B , 39 (2011).
[45] Y. Feng, Y.F. Lin, J. Zhao and F. Wang, Phys. Lett. B , 136549 (2021).